A mass-conserving pressure-based method for two-phase flows with phase change

By N. Scapin∗, A. Shahmardi∗, W. H. R. Chan, S. S. Jain, S. Mirjalili, M. Pelanti‡ AND L. Brandt∗†

We propose a mass-conserving numerical method for compressible two-phase flows with phase change, with a focus on the ability to model wetting. The algorithm employs a four-equation diffuse-interface formulation, which assumes instantaneous kinetic, mechanical, and thermal equilibrium, and allows for chemical disequilibrium between the two phases, hence phase change. In order to target boiling flows at low speeds, we leverage a pressure-based method developed in our previous work (Demou *et al.* 2022). This approach allows us to treat acoustic effects implicitly and account for compressibility and complex thermodynamics. Here, we first introduce an augmented four-equation formulation that ensures discrete mass conservation in the absence of phase change. Next, we add interface regularization to improve the accuracy of the topological description. Finally, a mass-conserving contact-angle boundary condition is implemented. The new implementation is validated against different benchmarks showing exact mass conservation for both phases in the absence of phase change and exact total mass conservation when phase change is activated. Finally, we present preliminary results on a vapor bubble detaching from a heated wall for different surface properties.

1. Introduction

One way to meet the rising global energy demand in a sustainable manner is to improve phase change heat transfer (Attinger D. *et al.* 2014). Phase change is the most efficient way to increase heat transfer, since latent heat is typically much larger than sensible heat. The recent development of micro- and nanotechnologies has made the high-resolution control of surface texture and chemistry feasible over different length scales (Attinger D. *et al.* 2014; Liang, G., & Mudawar, I. 2019). These complex surfaces may significantly affect several processes of high practical interest, e.g., boiling, evaporation, and condensation. In a field where experiments are complex, a deep understanding of the mechanisms underlying wetting and multiphase flows with phase change may be achieved through high-fidelity numerical simulations. The objective of the present project is, therefore to investigate the potential of the diffuse-interface method for simulations of compressible multiphase flows with phase change in more realistic configurations, in particular accounting for the contact-line dynamics.

2. Mathematical model

We describe gas-liquid flows by a diffuse-interface four-equation model (Lund 2012; Le Martelot *et al.* 2014; Demou *et al.* 2022), which belongs to the class of Baer–Nunziato

∗ FLOW, Department of Engineering Mechanics, KTH, Sweden
‡ ENSTA Paris - Institut Polytechnique de Paris, France
† Department of Energy and Process Engineering, NTNU, Norway

(Baer & Nunziato 1986) models. We assume instantaneous kinetic, mechanical, and thermal equilibrium, but we account for chemical disequilibrium and thus for phase change. The model also includes viscous stresses, surface tension, heat conduction, and gravity effects. We denote hereafter with α_k, ρ_k, and $\mathcal{E}_k$ the volume fraction, density, and internal energy per unit volume of phase k, where $k = 1, 2$. Moreover, p, T, and $\vec{u}$ indicate the pressure, temperature, and velocity field, respectively. The mixture density is $\rho = \alpha_1\rho_1 + \alpha_2\rho_2$, and the mixture internal energy per unit volume $\mathcal{E} = \alpha_1\mathcal{E}_1 + \alpha_2\mathcal{E}_2$. We denote with E the total energy of the mixture, which is defined as $E = \mathcal{E} + \rho|\vec{u}|^2/2$. In the conservative form, the model reads (Demou *et al.* 2022)

$$\partial_t(\alpha_1\rho_1) + \vec{\nabla}\cdot(\alpha_1\rho_1\vec{u}) = \mathcal{M}, \tag{2.1a}$$

$$\partial_t(\alpha_2\rho_2) + \vec{\nabla}\cdot(\alpha_2\rho_2\vec{u}) = -\mathcal{M}, \tag{2.1b}$$

$$\partial_t(\rho\vec{u}) + \vec{\nabla}\cdot(\rho\vec{u}\otimes\vec{u} + p\vec{\vec{I}}) = \vec{\nabla}\cdot\vec{\vec{\tau}} + \vec{\Sigma} + \rho\,\vec{\mathrm{g}}\,, \text{ and} \tag{2.1c}$$

$$\partial_t E + \vec{\nabla}\cdot((E+p)\vec{u}) = \vec{\nabla}\cdot(\vec{\vec{\tau}}\cdot\vec{u}) + K + \vec{\Sigma}\cdot\vec{u} + \rho\vec{\mathrm{g}}\cdot\vec{u}\,. \tag{2.1d}$$

Here $\vec{\mathrm{g}}$ denotes the gravity acceleration, and $\vec{\vec{\tau}}$ is the viscous stress tensor, for which we assume a Newtonian constitutive relation,

$$\vec{\vec{\tau}} = \mu[\,(\vec{\nabla}\vec{u} + \vec{\nabla}\vec{u}^{\mathrm{T}}) - \tfrac{2}{3}(\vec{\nabla}\cdot\vec{u})\vec{\vec{I}}\,], \tag{2.2}$$

where $\mu = \alpha_1\mu_1 + \alpha_2\mu_2$, with μ_k denoting the dynamic viscosity of phase k. Moreover, $\vec{\Sigma}$ is the surface tension force,

$$\vec{\Sigma} = \sigma\kappa\vec{\nabla}\alpha_1\,, \tag{2.3}$$

where σ is the surface tension coefficient and $\kappa = -\vec{\nabla}\cdot\left(\frac{\vec{\nabla}\alpha_1}{|\vec{\nabla}\alpha_1|}\right)$ the local curvature. The heat conduction K is expressed by Fourier law,

$$K = \vec{\nabla}\cdot(\lambda_c\vec{\nabla}T)\,, \tag{2.4}$$

where the mixture thermal conductivity is $\lambda_c = \alpha_1\lambda_{c1} + \alpha_2\lambda_{c2}$, with λ_{ck} denoting the thermal conductivity of phase k. Note that $\mathcal{M}$ is the mass transfer term, which is expressed as a relaxation term proportional to the difference in chemical potential as

$$\mathcal{M} = \nu(g_2 - g_1), \tag{2.5}$$

where ν is a chemical relaxation parameter. A formulation of the model [Eq. 2.1] in terms of the primitive variables α_1, p, T, and $\vec{u}$ was proposed in Demou *et al.* (2022), as a basis for a pressure-correction algorithm, more suited for low-Mach-number problems, in particular boiling flows. Here we employ a similar pressure-correction method for the conservative formulation for the transport equations of the two masses and the momentum to guarantee the conservation of ρ_k exactly (Jain *et al.* 2020; Jain 2022). We therefore propose an augmented four-equation model, solving for the five variables $(\alpha_1\rho_1, \alpha_2\rho_2, \rho\vec{u}, p, T)$ and consisting of the transport equations for the phase masses [Eq.2.1a), (2.1b)], the mixture momentum equation [Eq.2.1c], and the pressure and temperature equation derived in Demou *et al.* (2022),

$$\partial_t p + \vec{u}\cdot\vec{\nabla}p + \rho\,c_{pT}^2\vec{\nabla}\cdot\vec{u} = \mathcal{S}_p\,\mathcal{M} + \mathcal{S}_p^e(\vec{\nabla}\vec{u} : \vec{\vec{\tau}} + K)\,, \text{ and} \tag{2.6a}$$

$$\partial_t T + \vec{u}\cdot\vec{\nabla}T + \frac{\rho c_{pT}^2 T}{C_{p1}+C_{p2}}\left(\frac{C_{p1}\Gamma_1}{\rho_1 c_1^2} + \frac{C_{p2}\Gamma_2}{\rho_2 c_2^2}\right)\vec{\nabla}\cdot\vec{u} = \mathcal{M}\mathcal{S}_T + \mathcal{S}_T^e(\vec{\nabla}\vec{u} : \vec{\vec{\tau}} + K), \tag{2.6b}$$

where the speed of sound is (Flåtten & Lund 2011; Pelanti & Shyue 2019)

$$\frac{1}{c_{pT}^2} = \frac{1}{c_p^2} + \frac{\rho T C_{p1} C_{p2}}{C_{p1}+C_{p2}} \left(\frac{\Gamma_2}{\rho_2 c_2^2} - \frac{\Gamma_1}{\rho_1 c_1^2} \right)^2, \tag{2.7}$$

and $C_{pk} = \alpha_k \rho_k \kappa_{pk}$ (extensive heat capacities), where $\kappa_{pk} = \frac{\partial h_k}{\partial T_k}\big|_{p_k} = T_k \frac{\partial s_k}{\partial T_k}\big|_{p_k}$. Moreover, the forcing terms read

$$\mathcal{S}_T = \tfrac{1}{D_T} \left[\left(\tfrac{\chi_2}{\Gamma_2} - \tfrac{\chi_1}{\Gamma_1} \right) (\alpha_1\zeta_1\rho_2 + \alpha_2\zeta_2\rho_1) + \left(\tfrac{\rho_1 c_1^2}{\Gamma_1} - \tfrac{\rho_2 c_2^2}{\Gamma_2} \right) (\alpha_1\zeta_1 + \alpha_2\zeta_2) + \left(\tfrac{\alpha_1}{\Gamma_1} + \tfrac{\alpha_2}{\Gamma_2} \right) (\rho_2 - \rho_1) \right], \tag{2.8a}$$

$$\mathcal{S}_p = \tfrac{1}{D_T} \left[\left(\tfrac{\chi_1}{\Gamma_1} - \tfrac{\chi_2}{\Gamma_2} \right) (\alpha_1\phi_1\rho_2 + \alpha_2\phi_2\rho_1) + \left(\tfrac{\rho_2 c_2^2}{\Gamma_2} - \tfrac{\rho_1 c_1^2}{\Gamma_1} \right) (\alpha_1\phi_1 + \alpha_2\phi_2) \right], \text{ and} \tag{2.8b}$$

$$\mathcal{S}_T^e = -\frac{1}{D_T} (\alpha_1\rho_2\zeta_1 + \alpha_2\rho_1\zeta_2), \quad \mathcal{S}_p^e = \frac{1}{D_T} (\alpha_1\phi_1\rho_2 + \alpha_2\phi_2\rho_1), \tag{2.8c}$$

with

$$D_T = \alpha_1\alpha_2 \left(\frac{\rho_1 c_1^2}{\Gamma_1} - \frac{\rho_2 c_2^2}{\Gamma_2} \right) (\phi_1\zeta_2 - \phi_2\zeta_1) + \left(\frac{\alpha_1}{\Gamma_1} + \frac{\alpha_2}{\Gamma_2} \right) (\alpha_1\phi_1\rho_2 + \alpha_2\phi_2\rho_1). \tag{2.8d}$$

Here ϕ_k, ζ_k, and the Grüneisen coefficient Γ_k are defined as

$$\phi_k = \left(\frac{\partial \rho_k}{\partial T_k} \right)_{p_k}, \quad \zeta_k = \left(\frac{\partial \rho_k}{\partial p_k} \right)_{T_k}, \quad \text{and } \Gamma_k = \left(\frac{\partial p_k}{\partial \mathcal{E}_k} \right)_{\rho_k}. \tag{2.9}$$

The model is closed with an equation of state for each phase, e.g., by pressure and temperature relations $p_k(\mathcal{E}_k, \rho_k)$ and $T_k(\mathcal{E}_k, \rho_k)$, $k = 1, 2$. The mixture equation of state is determined by these and the thermodynamic constraints $p_1 = p_2 = p$, $T_1 = T_2 = T$. Our numerical method can use arbitrary equations of state; nevertheless, for the numerical experiments presented here we have used the Noble-Abel stiffened Gas equation of state for both phases as in Le Métayer & Saurel (2016).

2.1. *Interface regularization*

One well-known drawback of diffuse-interface methods is the spreading of the interface over many computational cells. To maintain the interface sharpness, we therefore apply an anti-diffusion technique (Tiwari *et al.* 2013; Jain *et al.* 2020; Mirjalili *et al.* 2020). Following in particular the approach proposed in Jain (2022), we include interface regularization in the mass and momentum equations of our augmented 4-equation model. The final form of the mathematical model is

$$\partial_t(\alpha_1\rho_1) + \vec{\nabla} \cdot (\alpha_1\rho_1\vec{u}) = \mathcal{M} + \vec{\nabla} \cdot \vec{\mathcal{R}}(\alpha_1, \rho_1) + \mathcal{L}_{w,1}, \tag{2.10a}$$

$$\partial_t(\alpha_2\rho_2) + \vec{\nabla} \cdot (\alpha_2\rho_2\vec{u}) = -\mathcal{M} + \vec{\nabla} \cdot \vec{\mathcal{R}}(\alpha_2, \rho_2) + \mathcal{L}_{w,2}, \tag{2.10b}$$

$$\partial_t(\rho\vec{u}) + \vec{\nabla} \cdot (\rho\vec{u} \otimes \vec{u} + p\vec{\vec{I}}) = \vec{\nabla} \cdot \vec{\vec{\tau}} + \vec{\Sigma} + \rho\,\vec{g} + \vec{\nabla} \cdot [(\rho_1 - \rho_2)\vec{\mathcal{R}}(\alpha_1, \rho_1)], \tag{2.10c}$$

$$\partial_t p + \vec{u} \cdot \vec{\nabla} p + \rho\, c_{pT}^2 \vec{\nabla} \cdot \vec{u} = \mathcal{S}_p\, \mathcal{M} + \mathcal{S}_p^e (\vec{\nabla}\vec{u} : \vec{\vec{\tau}} + K), \text{ and} \tag{2.10d}$$

$$\partial_t T + \vec{u} \cdot \vec{\nabla} T + \frac{\rho c_{pT}^2 T}{C_{p1}+C_{p2}} \left(\frac{C_{p1}\Gamma_1}{\rho_1 c_1^2} + \frac{C_{p2}\Gamma_2}{\rho_2 c_2^2} \right) \vec{\nabla} \cdot \vec{u} = \mathcal{M}\mathcal{S}_T + \mathcal{S}_T^e (\vec{\nabla}\vec{u} : \vec{\vec{\tau}} + K), \tag{2.10e}$$

where the regularization term $\vec{\mathcal{R}}$ is defined as

$$\vec{\mathcal{R}}(\alpha_k, \rho_k) = \Xi\, \varepsilon_i\, \rho_k \vec{\nabla}\alpha_k - \frac{\Xi \rho_k}{4}\left[1 - \tanh^2\left(\frac{\psi_k}{2\varepsilon_i}\right)\right]\vec{n}_k\,, \quad k = 1, 2, \tag{2.11}$$

where

$$\psi_k = \varepsilon_i \ln\left(\frac{\alpha_k + \epsilon}{1 - \alpha_k + \epsilon}\right), \tag{2.12}$$

with ε_i denoting the interface thickness, $\Xi = \Gamma_v |\vec{u}_{max}|$ denoting the regularization velocity, Γ_v is a velocity scale, and ϵ is a small tolerance that is set equal to $2 \cdot 10^{-16}$. Moreover, $\vec{n}_k = \vec{\nabla}\psi_k / |\vec{\nabla}\psi_k|$. The terms $\mathcal{L}_{w,k}$ are added to the right-hand side of Eqs. (2.10a)-(2.10b) to enforce mass conservation in the presence of non-zero flux boundary conditions at the solid wall, as detailed in Section 2.2.

2.2. *Contact-line treatment*

A static contact-angle boundary condition is enforced as a condition on the wall-normal gradient of $(\alpha_k \rho_k)$, with $k = 1, 2$ (Jacqmin 1999). Note that unlike previous studies (Jacqmin 1999; Ziyang *et al.* 2022), we impose a boundary condition on the mass of both phases rather than on the volume fraction since only the former is a conserved quantity in the presence of local density variations. Here, we adopt the following expression to impose the equilibrium contact angle $\theta_{eq,k}$

$$\nabla(\alpha_k \rho_k) \cdot \vec{n} = \frac{\rho_k}{\varepsilon_i} f_{w,k} \cos(\theta_{eq,k}), \tag{2.13}$$

where $f_{w,k} = 6\alpha_k(1 - \alpha_k)$ is a kernel function that is non-zero only at the interface. Note that $\theta_{eq,2} = \pi - \theta_{eq,1}$ and the expression above imply a zero flux boundary condition only if $\theta_{eq} = \pi/2$. To relax this constraint and to enforce mass conservation when $\theta_{eq} \neq \pi/2$, we employ a Lagrange multiplier $\mathcal{L}_{w,i}$. This approach, proposed in the context of incompressible flows in Ziyang *et al.* (2022), is here adapted for compressible flows with phase change. Assuming $\mathcal{L}_{w,k} = q_k(t)\mathcal{W}(\alpha_k, \rho_k)$, with $q_k(t)$ a space-independent function and $\mathcal{W}(\alpha_k, \rho_k) = \rho_k f_{w,k}$ a kernel function, an expression for $q_k(t)$ can be obtained by integrating Eqs. (2.10a) and (2.10b) over the volume and enforcing total conservation of the mass of each phase,

$$q_k(t) = -\frac{1}{\displaystyle\int_V 6\rho_k \alpha_k (1 - \alpha_k) dV} \int_V \nabla \cdot \vec{\mathcal{R}}(\alpha_k, \rho_k) dV. \tag{2.14}$$

When phase change is included, m_k should not be conserved; in this case, the multiplier enables us to achieve exact total mass conservation, as discussed in Section 2.3.

2.3. *Phase change*

The phase change term $\mathcal{M}$, given by Eq. (2.5), is implemented with an operator splitting technique. We first solve the governing equations without $\mathcal{M}$ and obtain intermediate values for $(\alpha_k \rho_k)^{l,*}$, $T^{l,*}$ and $p^{l,*}$, where $l = 1, 2, 3$ denotes the Runge-Kutta stage. The independent variables are updated at the end of each stage using the non-iterative

strategy proposed in Pelanti (2022) as

$$(\alpha_1\rho_1)^{l,n+1} = (\alpha_1\rho_1)^{l,*} + \frac{g_2^{l,*} - g_1^{l,*}}{K_g}\left(1 - \exp\left(-\nu K_g \Delta t\right)\right), \tag{2.15a}$$

$$p^{l,n+1} = p^{l,*} + \mathcal{S}_p \frac{g_2^{l,*} - g_1^{l,*}}{K_g}\left(1 - \exp\left(-\nu K_g \Delta t\right)\right), \text{ and} \tag{2.15b}$$

$$T^{l,n+1} = T^{l,*} + \mathcal{S}_T \frac{g_2^{l,*} - g_1^{l,*}}{K_g}\left(1 - \exp\left(-\nu K_g \Delta t\right)\right), \tag{2.15c}$$

where $K_g = 1/\xi_1^{l,*} + 1/\xi_2^{l,*}$ and $1/\xi_k^{l,*} = (-1)^{k-1}\mathcal{S}_p/\rho_k - s_k\mathcal{S}_T$ for $k = 1, 2$. Note that ρ is obviously invariant during the mass transfer step and, therefore exact global mass conservation is enforced by updating $(\alpha_2\rho_2)^{l,n+1} = \rho^{l,n+1} - (\alpha_1\rho_1)^{l,n+1}$. Our numerical method is capable of handling arbitrary values of the relaxation rate ν, which is in general a function of the thermodynamic variables. For the numerical experiments presented here, we have assumed $\nu \to +\infty$, i.e., instantaneous mass transfer (zero relaxation time).

3. Numerical details

Equations (2.10*a*) (2.10*e*) are discretized in space on a Cartesian grid with uniform spacing along the three directions, i.e., $\Delta x = l_x/N_x$, $\Delta y = l_y/N_y$, and $\Delta z = l_z/N_z$, where l_x, l_y, and l_z are the domain lengths and N_x, N_y, and N_z the number of grid points. A staggered arrangement is chosen for the velocity field, whereas all the other variables are defined at the cell centers. Unless otherwise stated, we set $\varepsilon_i = 0.51\Delta x$ and $\Gamma_v = 5$ in Eq. (2.11). This value of Γ_v is chosen to avoid excessive interface smearing during the mass transfer. The spatial operators are discretized in divergence form using a second-order accurate finite difference scheme. The equations are marched in time with a third-order low-storage Runge-Kutta method. More details are given in Demou *et al.* (2022).

4. Numerical experiments

4.1. *Rising bubble*

To assess the ability of the proposed methodology to capture topological changes, we consider the well-established test case of a rising bubble (Hysing *et al.* 2009). The numerical solution obtained here is compared with the reference solution in Hysing *et al.* (2009), in terms of bubble rising velocity and shape, in addition to the assessment of the mass conservation. By introducing as reference length and velocity $l_r = d_0$ and $u_r = \sqrt{|\vec{g}|d_0}$, with d_0 the initial bubble diameter, as gas and liquid densities $\rho_{g,r}$ and $\rho_{l,r}$, as gas and liquid dynamic viscosities $\mu_{g,r}$ and $\mu_{l,r}$, and as surface tension σ, we can define the five physical dimensionless parameters which govern the problem: $Re = \rho_{g,r}u_r d_0/\mu_{g,r}$, the Weber number $We = \rho_{g,r}u_r^2 d_0/\sigma$, the Froude number $Fr = u_r^2/(|\vec{g}|d_0)$, the density and the viscosity ratios $\lambda_\rho = \rho_{l,r}/\rho_{g,r}$ and $\lambda_\mu = \mu_{l,r}/\mu_{g,r}$. In this work, simulations are conducted with $Re = 35$, $We = 1$, $Fr = 1$, $\lambda_\rho = 1000$, and $\lambda_\mu = 100$. The domain consists of a two-dimensional liquid column of size $l_x = 2d_0$, $l_y = 4d_0$, with a bubble initially placed at $(x_{c0}, y_{c0}) = (d_0, d_0)$. The top and bottom boundaries are no-slip non-moving walls, while periodic conditions are prescribed in the horizontal directions. The initial velocity field is zero and the pressure is uniform. Four grid resolutions are examined: $\mathrm{N}_x \times \mathrm{N}_y$=[32×64, 64×128, 128×256, 256×512], with a constant time step $\Delta t\sqrt{|\vec{g}|/d_0} = 3{\cdot}10^{-4}$,

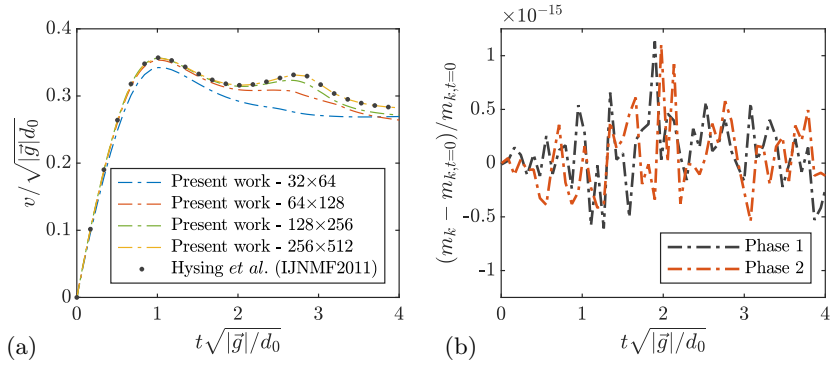

Figure 1. Rising bubble test case: (a) rising velocity of the bubble center of mass from the simulations at the different resolutions indicated, (b) relative variation of the mass of each phase over time.

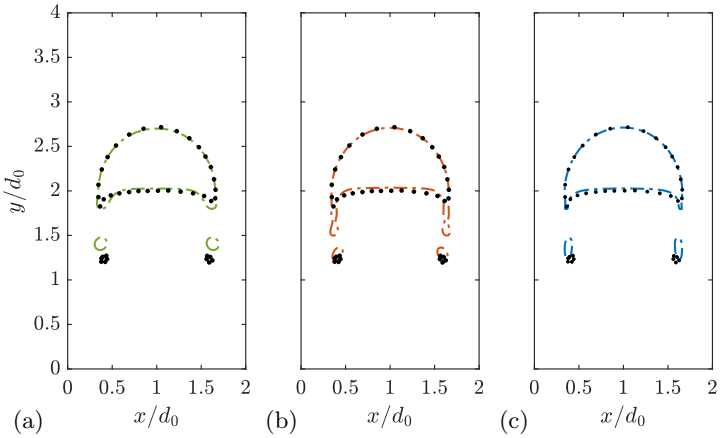

Figure 2. Interface of the rising bubble at time $t\sqrt{|\vec{g}|/d_0} = 3$ for different grid resolutions: (a) $N_x \times N_y = 64 \times 128$, (b) 128×256, and (c) 256×512. The dotted black line represents the reference solution taken by Hysing *et al.* (2009).

the largest time step ensuring a stable time integration for the highest grid resolution (i.e., 256×512), adopted to have the same time discretization error in all the cases. Figure 1(a) displays the rising velocity of the bubble center of mass. As the grid is refined, the numerical solutions approach the reference data, with an excellent agreement for the grid with 256×512 points. The temporal evolution of the relative mass variations are reported in figure 1(b) for both phases. Mass conservation is achieved up to machine precision as a consequence of the conservative discretization of Eqs. (2.10a)- (2.10b). Figure 2 reports the bubble shape at time $t\sqrt{\vec{g}/d_0} = 3$, which converges to the one reported in Hysing *et al.* (2009) when increasing the resolution. Small differences are observed for the two "satellite bubbles" [see Fig. 2], which are an indication of underresolution of surface tension forces in this two-dimensional simulation. These two bubbles display a larger volume and a different orientation with respect to the reference solution obtained with a geometric volume-of-fluid method. Such deviations are, however, small and within the expected differences when two different numerical methods are compared.

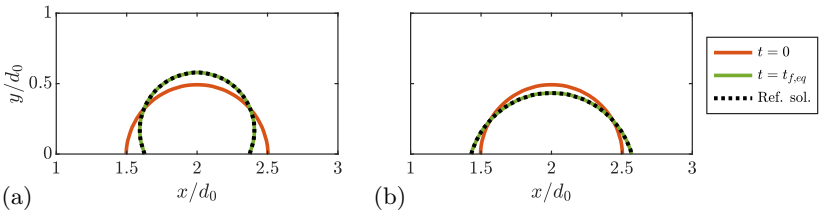

Figure 3. Static contact-line test case. Bubble shape for two equilibrium contact angles: (a) $\theta = 45^o$, (b) $\theta = 135^o$. The dotted black lines represent the shape computed with Eqs. (4.1).

4.2. *Static contact line*

As the second test case, we consider a semicircular bubble of diameter d_0 sliding on a horizontal wall. The wall is either hydrophobic or hydrophilic, i.e., with equilibrium contact angle $\theta_{eq} > 90^o$ and $\theta_{eq} < 90^o$. In both cases, the initial contact angle of the bubble is prescribed equal to $\theta_{eq} = 90^o$, and, therefore the bubble relaxes towards the desired θ_{eq} after a transient. The case setup consists of a two-dimensional domain of dimension $4d_0 \times 2d_0$ with the bubble held at $[x_{c0}, y_{c0}] = [2d_0, 0]$. The domain is discretized with $N_x \times N_z = 128 \times 64$ grid points. Periodic boundary conditions are applied along the horizontal direction and no-slip along the horizontal boundaries. The dimensionless physical parameters defining the problem are $Re = 25$, $We = 0.1$, $\lambda_\rho = 1000$, $\lambda_\mu = 50$, and the thermal conductivity ratios $\lambda_k = 20$; gravity is absent, i.e., $Fr = \infty$. Note that the effect of gravity is neglected. Figure 3 reports the initial and the equilibrium shape of the bubble for a wall chemistry yielding an equilibrium contact angle $\theta_{eq} = 45^o$ and $\theta_{eq} = 135^o$. As expected, the bubble relaxes towards the desired shape with the prescribed contact angle. The final radius r_d/d_0, the height H_d/d_0, and the spreading length l_d/d_0 can be computed analytically as proposed in Ziyang *et al.* (2022),

$$\frac{r_d}{d_0} = \frac{1}{2}\sqrt{\frac{\pi/2}{\theta - \sin(\theta_{eq})\cos(\theta_{eq})}}, \quad \frac{H_d}{d_0} = \frac{r_d}{d_0}(1-\cos(\theta_{eq})), \quad \text{and} \quad \frac{l_d}{d_0} = 2\frac{r_d}{d_0}\sin(\theta_{eq}). \tag{4.1}$$

We therefore consider different values of θ_{eq} and display in Figure 4(a) the resulting h_d/d_0 and l_d/d_0 versus the analytical prediction in Eqs. (4.1) and confirm that a very good agreement is obtained for all the cases. Finally, note that owing the use of the Lagrange multiplier discussed in Section 2.2, the mass of the two phases is conserved to machine precision [see Figure 4(b)].

4.3. *Detaching bubble from a superheated wall*

To demonstrate the potential of the method, we consider the case of a detaching bubble from a solid wall for different wettabilities and wall temperatures, in particular, three equilibrium contact angles, $\theta_{eq} = [45^o, 90^o, 120^o]$, and two superheating temperatures, $\Delta T = 5, 15$ K. Note that these values correspond to a Jacob number $Ja = C_{p,1}\Delta T/\Delta h_{lv}$, with Δh_{lv} the latent heat, of 0.025 and 0.085. We consider a two-dimensional domain of size $7d_0 \times 3.5d_0$, where d_0 is the initial diameter of a semicircular bubble initially placed at $(x_c0, y_c0) = [3.5d_0, 0]$. The domain is discretized with $N_x \times N_y = 256 \times 128$ grid points. We set $Re = 125$, $We = 1$, $Fr = 1$, $\lambda_\rho = 1103$, $\lambda_\mu = 50$, and $\lambda_k = 20$, which correspond to the case of a mixture of water and its vapor at ambient pressure. The velocity field is initially set to zero, and the initial temperature is equal to the saturation temperature at the initial pressure. Periodic boundary conditions are applied

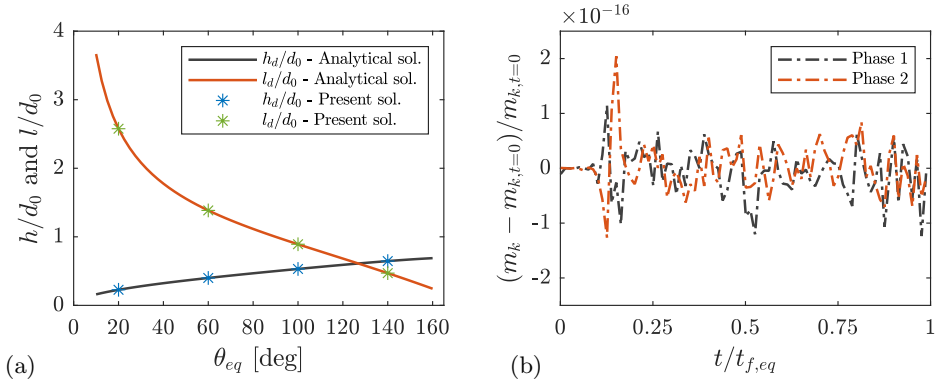

Figure 4. *(a)*: Bubble height h_d/d_0 and spreading length l_d/d_0 at equilibrium for different contact angles θ_{eq}.*(b)*: Relative mass variations versus time of both phases for the case $\theta_{eq} = 45^{\text{o}}$.

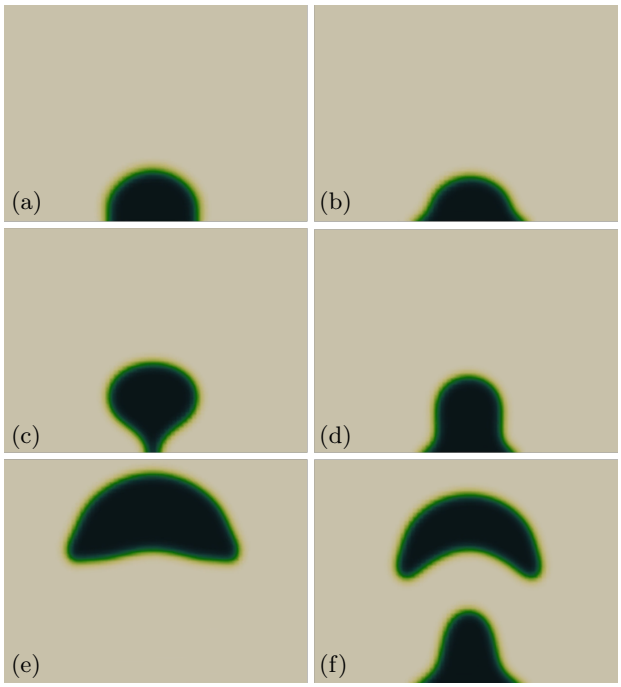

Figure 5. Rising boiling bubble over a supersaturated wall for $Ja = 0.025$ at $t\sqrt{\vec{g}/l_y} = 0.25 - 1 - 2$. (a)-(c)-(e) Results for a contact angle $\theta_{eq} = 90^{\text{o}}$. (b)-(d)-(f) Results for $\theta_{eq} = 120^{\text{o}}$.

along the x direction, no-slip at the bottom wall, and outflow at the upper wall. In Figure 5 we show plots of the vapor volume fraction at three different times for the neutral and hydrophobic walls. In particular, we observe a complete detachment of the bubble from the wall for the case $\theta = 90^{\text{o}}$ without breakup; whereas for $\theta = 120^{\text{o}}$ (hydrophobic case), we observe stretching of the bubble and its breakup. The upper part of the bubble departs from the wall and the lower part remains attached to the heated

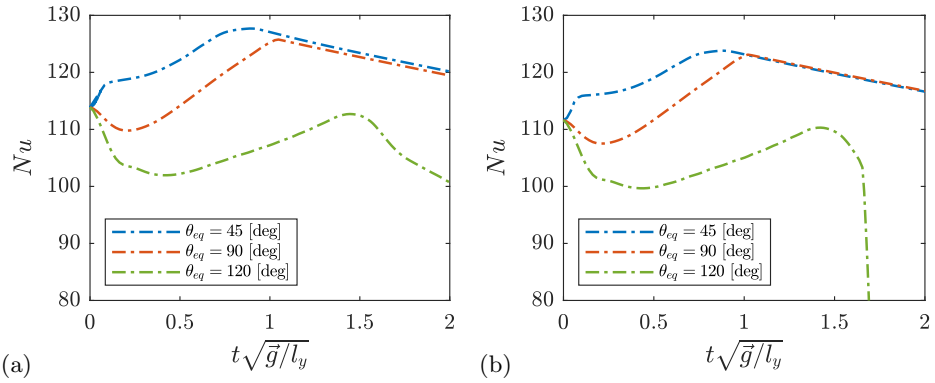

Figure 6. Nusselt number at the bottom wall, $Nu = ql_y/(k_1\Delta T)$, for (a) $Ja = 0.025$ and (b) $Ja = 0.085$. Three different static contact angles are investigated, $\theta_{eq} = 45^{\circ}, 60^{\circ}$ and 120°. The reference time scale is the free-fall time $t_{ff} = \sqrt{l_y/\vec{g}}$.

surface and grows. The wall wettability also determines the heat flux, i.e., the Nusselt number Nu, at the bottom wall, displayed in figure 6. The Nusselt number is larger for hydrophilic surfaces due to the larger liquid-wall surface area, which promotes fast bubble detachment. Conversely, the detachment is slower on hydrophobic walls since the vapor phase experiences a longer residence time close to the heated wall with reduced heat transfer (because of the lower thermal conductivity of the vapor). The lowest residence time at the bottom wall is experienced for $\theta_{eq} = 45^{\circ}$, which explains the increase of Nu at the earlier stages. This time progressively increases with θ_{eq}, and therefore Nu initially decreases until $t\sqrt{\vec{g}/l_y} \approx 0.25 - 0.50$ for $\theta_{eq} = 90^{\circ} - 120^{\circ}$, whereas it increases once the bubble detaches. In all the cases, the value of Nu reaches a maximum value, which is similar for $\theta = 45^{\circ} - 90^{\circ}$ and smaller for $\theta = 120^{\circ}$ given the smaller liquid-wall contact area. After, Nu slowly decreases for $\theta_{eq} = 45^{\circ}$ and 90° for both Ja. Conversely, for $\theta_{eq} = 120^{\circ}$, the increase in the superheating temperature leads to vapor production at the heated wall with a reduction of the heat flux at $t\sqrt{\vec{g}/l_y} \approx 1.5$, which is most pronounced for $Ja = 0.085$.

5. Conclusions

We have developed a mass-conserving pressure-based method for two-phase compressible flows with phase change based on a pressure-temperature-equilibrium single-velocity model. An anti-diffusion interface sharpening technique has been applied to improve the accuracy of the topological description. Static contact-angle boundary conditions have been implemented by using a Lagrange multiplier to ensure mass conservation. In the future, we aim to employ the proposed computational model to gain fundamental understanding of phase change over patterned surfaces, resolving the contact-line dynamics and the Marangoni stresses generated by the local variations of the surface tension due to temperature gradients.

Acknowledgments

The authors acknowledge use of computational resources from the Yellowstone cluster awarded by the National Science Foundation to CTR, from SNIC (Swedish National Infrastructure for Computing) and from the National Infrastructure for High-Performance Computing and Data Storage in Norway (project no. NN9561K).

REFERENCES

Attinger D., Frankiewicz C., Betz A. R., Schutzius T. M., Ganguly R., Das A., Kim C.-J. & Megaridis C. M. 2014 Surface engineering for phase change heat transfer. *MRS Energy Sustain.* **1**, E4.

Baer, M. R., & Nunziato, J. W. 1986, A two-phase mixture theory for the deflagration-to-detonation transition (DDT) in reactive granular materials. *Int. J. Multiphas. Flow.* **12**, 861–889.

Demou, A. D., Scapin, N., Pelanti, M., & Brandt, L. 2022 A pressure-based diffuse interface method for low-Mach multiphase flows with mass transfer. *J. Comput. Phys.* **448**, 110730.

Fltten, T., & Lund, H. 2011 Relaxation two-phase flow models and the subcharacteristic condition. *Math. Models Methods Appl. Sci.* **21**, 2379–2407.

Hysing, S. R., Turek, S., Kuzmin, D., Parolini, N., Burman, E., Ganesan, S., & Tobiska, L. 2009 Quantitative benchmark computations of twodimensional bubble dynamics. *Int. J. Numer Meth. Fl.* **60**, 1259–1288.

Liang, G., & Mudawar, I. 2019 Review of pool boiling enhancement by surface modification. *Int. J. Heat Mass Tran.* **128**, 892–933.

Jacqmin, D. 1999 Calculation of two-phase NavierStokes flows using phase-field modeling. *J. Comput. Phys.* **155**, 96–127.

Jain, S. S. 2022 Accurate conservative phase-field method for simulation of two-phase flows. *J. Comput. Phys.* **418**, 109606.

Jain, S. S., Mani, A., & Moin, P. 2020 A conservative diffuse-interface method for compressible two-phase flows. *J. Comput. Phys.* **418**, 109606.

Le Martelot, S., Saurel, R., & Nkonga, B. 2014 Towards the direct numerical simulation of nucleate boiling flows. *Int. J. Multiphas. Flow.* **66**, 62–78.

Le Métayer,O. & Saurel, R. 2016 The Noble-Abel stiffened-gas equation of state. *Phys. Fluids.* **28**, 046102.

Lund, H. 2012 A hierarchy of relaxation models for two-phase flow. *SIAM J. Appl. Math.* **72**, 1713-1741.

Mirjalili, S., Ivey, C., & Mani, A. 2020 A conservative diffuse interface method for two-phase flows with provable boundedness properties. *J. Comput. Phys.* **401**, 109006.

Pelanti, M. 2022 Arbitrary-rate relaxation techniques for the numerical modeling of compressible two-phase flows with heat and mass transfer. *Int. J. Multiphas. Flow.* **153**, 104097.

Pelanti, M., & Shyue, K. M. 2019 A numerical model for multiphase liquid-vapor-gas flows with interfaces and cavitation. *Int. J. Multiphas. Flow.* **113**, 208–230.

Tiwari, A., Freund, J. B., & Pantano, C. 2013 A diffuse interface model with immiscibility preservation. *J. Comput. Phys.* **252**, 290–309.

Ziyang H., Lin G., & Ardekani A. M. 2022 Implementing contact angle boundary conditions for second-order Phase-Field models of wall-bounded multiphase flows. *J. Comput. Phys.* **471**, 111619.